Noninvasive and localized neuronal delivery using short ultrasonic pulses and microbubbles

James J. Choi[a], Kirsten Selert[a], Fotios Vlachos[a], Anna Wong[a], and Elisa E. Konofagou[a,b,1]

[a]Department of Biomedical Engineering and [b]Department of Radiology, Columbia University, New York, NY 10032

Edited by Robert Langer, Massachusetts Institute of Technology, Cambridge, MA, and approved August 9, 2011 (received for review March 31, 2011)

Focused ultrasound activation of systemically administered microbubbles is a noninvasive and localized drug delivery method that can increase vascular permeability to large molecular agents. Yet the range of acoustic parameters responsible for drug delivery remains unknown, and, thus, enhancing the delivery characteristics without compromising safety has proven to be difficult. We propose a new basis for ultrasonic pulse design in drug delivery through the blood–brain barrier (BBB) that uses principles of probability of occurrence and spatial distribution of cavitation in contrast to the conventionally applied magnitude of cavitation. The efficacy of using extremely short (2.3 μs) pulses was evaluated in 27 distinct acoustic parameter sets at low peak-rarefactional pressures (0.51 MPa or lower). The left hippocampus and lateral thalamus were noninvasively sonicated after administration of Definity microbubbles. Disruption of the BBB was confirmed by delivery of fluorescently tagged 3-, 10-, or 70-kDa dextrans. Under some conditions, dextrans were distributed homogeneously throughout the targeted region and accumulated at specific hippocampal landmarks and neuronal cells and axons. No histological damage was observed at the most effective parameter set. Our results have broadened the design space of parameters toward a wider safety window that may also increase vascular permeability. The study also uncovered a set of parameters that enhances the dose and distribution of molecular delivery, overcoming standard trade-offs in avoiding associated damage. Given the short pulses used similar to diagnostic ultrasound, new critical parameters were also elucidated to clearly separate therapeutic ultrasound from disruption-free diagnostic ultrasound.

Focused ultrasound (FUS) and microbubble-based drug delivery systems (DDSs) can increase the dose of an agent in a target volume and has potential in applications such as blood–brain barrier (BBB) disruption for the treatment of neurological diseases (1, 2), molecular and viral treatment of tumors (3), gene therapy for treating heart conditions (4), and enhancement of renal ultrafiltration (5). In each method, biologically inert and preformed microbubbles, with a lipid or polymer shell, a stabilized gas core, and a diameter less than 10 μm, are systemically administered and subsequently exposed to noninvasively delivered FUS pulses. Microbubbles within the target volume are "acoustically activated" in a complex range of behaviors known as acoustic cavitation. In stable cavitation, the microbubbles expand and contract with the acoustic pressure rarefaction and compression over several cycles (6). This activity has been associated with a range of bioeffects including displacement of the vessel wall through dilation and contractions (7, 8). Large radial bubble expansions may induce inertial cavitation activity, which may lead to bubble collapse due to the inertia of the surrounding media and affect the vascular physiology (8). Each type and magnitude of cavitation activity results in distinct vascular bioeffects and are dictated by the ultrasonic pulse shape and sequence, the microbubble composition and distribution (9), and the in vivo environment the microbubbles circulate (8, 10). Selection of the exposure parameters is critical for effective drug delivery while minimizing side effects (11). Not accounting for these parameters may result in adverse effects even when a therapeutic effect is not intended, such as a previously observed increase in permeability with a diagnostic array (12) and, in severe situations, hemorrhage (13).

Currently, the mechanism of increased vascular permeability remains unknown, and thus enhancing drug delivery (i.e., spatial distribution, dose, and consistency) without inducing or exacerbating damage has been difficult. Pulse sequences used to drive cavitation in FUS-based DDSs typically consist of a peak-rarefactional pressure (PRP), a center frequency, and a pulse length (PL), emitted repeatedly at a pulse repetition frequency (PRF). The PRP significantly influences the type and magnitude of cavitation activity an exposed microbubble undergoes. Molecular delivery requires a minimum PRP known as the cavitation threshold, which is typically lower than 1 MPa (2, 14) and drops with the center frequency (15). Exposure of tissues above, but near, the threshold has so far yielded the most promising results with molecular delivery without any associated damage, as assessed using histological analysis (11). Further increasing the PRP enhances the dose delivered, but is also associated with a highly heterogeneous distribution within the focal volume and the onset of erythrocyte extravasations, hemorrhage, and neuronal damage (11, 16). Less understood is the effect different PLs have on delivery characteristics. Most of the aforementioned studies have used long PLs of 10 or 20 ms. However, recent work has shown that these PLs distribute the molecules heterogeneously throughout the target volume, with a greater accumulation near larger vessels (17). Reduction of the PL decreased not only the likelihood of BBB disruption, but also the delivered dose. Interestingly, lower PLs also exhibited a homogeneous and diffuse distribution of the molecule without high concentrations biased near the larger vessels. To date, FUS-based DDSs have been associated with a trade-off between efficacy and safety.

Results

Pulse-Sequence Design. The premise behind our pulse-sequence design was to minimize damage by maintaining the lowest possible magnitude of cavitation activity still able to modify vascular permeability. We aimed at simultaneously enhancing drug delivery distribution, dose, and consistency by increasing the number or cavitation events and distributing them as homogeneously throughout the length of the microvasculature as possible. To minimize damage, the PRP was 0.51 MPa or lower. A good distribution was aimed at through the use of extremely short PLs of 2.3 μs (Fig. S1). In order to compensate for the reduced dose a shorter PL may induce, we increased the frequency at which the pulses were emitted (e.g., PRFs of 100, 25, and 6.25 kHz). Finally, the need for microbubble replenishment was accounted for by grouping pulses into bursts, characterized by a burst length (BL) or number of

Author contributions: J.J.C. and E.E.K. designed research; J.J.C., K.S., F.V., and A.W. performed research; J.J.C. and F.V. analyzed data; and J.J.C. and E.E.K. wrote the paper.

The authors declare no conflict of interest.

This article is a PNAS Direct Submission.

Freely available online through the PNAS open access option.

[1]To whom correspondence should be addressed. E-mail: ek2191@columbia.edu.

This article contains supporting information online at www.pnas.org/lookup/suppl/doi:10.1073/pnas.1105116108/-/DCSupplemental.

pulses in a burst, which were emitted at a burst repetition frequency (BRF).

In Vivo BBB Disruption Experimental Setup. A stereotactic-based targeting system was used to focus ultrasound noninvasively through the intact scalp and skull (Fig. S2*A*) and to a region of interest (ROI) in the left hemisphere, which consisted of the left hippocampus and the lateral thalamus (Fig. S2 *B–E*). A 3.5-cycle (2.3-μs) pulse (Fig. S1) with a center frequency of 1.5 MHz was emitted for a duration of 11 min and in the presence of systemically administered microbubbles and fluorescently tagged dextran (molecular weight: 3 kDa). The normalized optical density (NOD), a measure of relative increase in fluorescence of the left (targeted) ROI to the right (nonsonicated control) ROI, was calculated for each mouse brain. Another value, the incidence of NOD increase, was calculated as the number of mice within an experimental group that had a NOD greater than a standard deviation above the sham group. Using these metrics, a wide range of ultrasonic parameters were evaluated for their ability to deliver dextran to the target ROI (Table S1).

Burst Repetition Frequency and Pulse Repetition Frequency. Emission of a continuous train of pulses at the PRP of 0.51 MPa and a PRF of 6.25, 25, and 100 kHz produced no significant increase in NOD (Fig. 1 *A*, *G*, and *M*). Only one out of three mice exposed to each condition underwent a NOD increase in the sonicated region, and in those instances, the fluorescence was of minute amplitude and mainly distributed around large vessels. Interestingly, increasing the "idle" time intervals of no FUS, which effectively reduced the total number of pulses emitted, increased the NOD in several instances. Optimal intervals were evaluated using a BL of 1,000 pulses and emitting them at BRFs of 0.1, 1, 2, 5, or 10 Hz, which corresponded to a burst repetition period of 10, 1, 0.5, 0.2, and 0.1 s, respectively. At 100-kHz PRF, significant increases in NOD were observed at BRFs of 2, 5, and 10 Hz, whereas no increase was observed at 0.1 and 1 Hz (Fig. 1*R*). At 25-kHz PRF, significant increases were observed at 1 and 2 Hz, whereas no increase was observed at 0.1, 5, and 10 Hz (Fig. 1*S*). At 6.25-kHz PRF, no significant increase was observed at any of the BRFs evaluated (Fig. 1*T*), although some mice had observable increases in fluorescence (Table S1). In general, the NOD increased with the interval between bursts and then decreased beyond a particular duration (Fig. 1*T*). Additionally, both the level and incidence of NOD decreased with the PRF. The NOD increase observed with a 100-kHz PRF and a 5-Hz BRF was significantly greater than under all other experimental sets of parameters (Fig. 1 *C* and *R*), and, therefore, these parameters, along with a 0.51-MPa PRP and a 1,000-pulse BL, were used in subsequent exposures, unless otherwise noted.

Pressure and Burst Length. The dependence of PRP on BBB disruption was evaluated in a sham and PRPs of 0.13, 0.25, 0.37, and 0.51 MPa (Fig. 2 *A–C*, *K*, and *L*). A significant increase in NOD was observed only at 0.51 MPa (Fig. 2*L*). Although 0.37 MPa had no significant increase in NOD, two out of three mice had detectable levels of fluorescence. Therefore, the PRP threshold for BBB disruption for a 3.5-cycle pulse was concluded to lie between 0.25 and 0.51 MPa. The effect of BL was evaluated from 1 to 1,000 pulses (Fig. 2 *D–K*). A single pulse did not produce a significant increase in NOD. The lowest BL with an incidence of NOD increase was five pulses and was observed in one out of three mice. Significant increases in NOD were observed at ten pulses and higher. Overall, increasing the number of pulses increased the likelihood and magnitude of NOD increase (Fig. 2*M*).

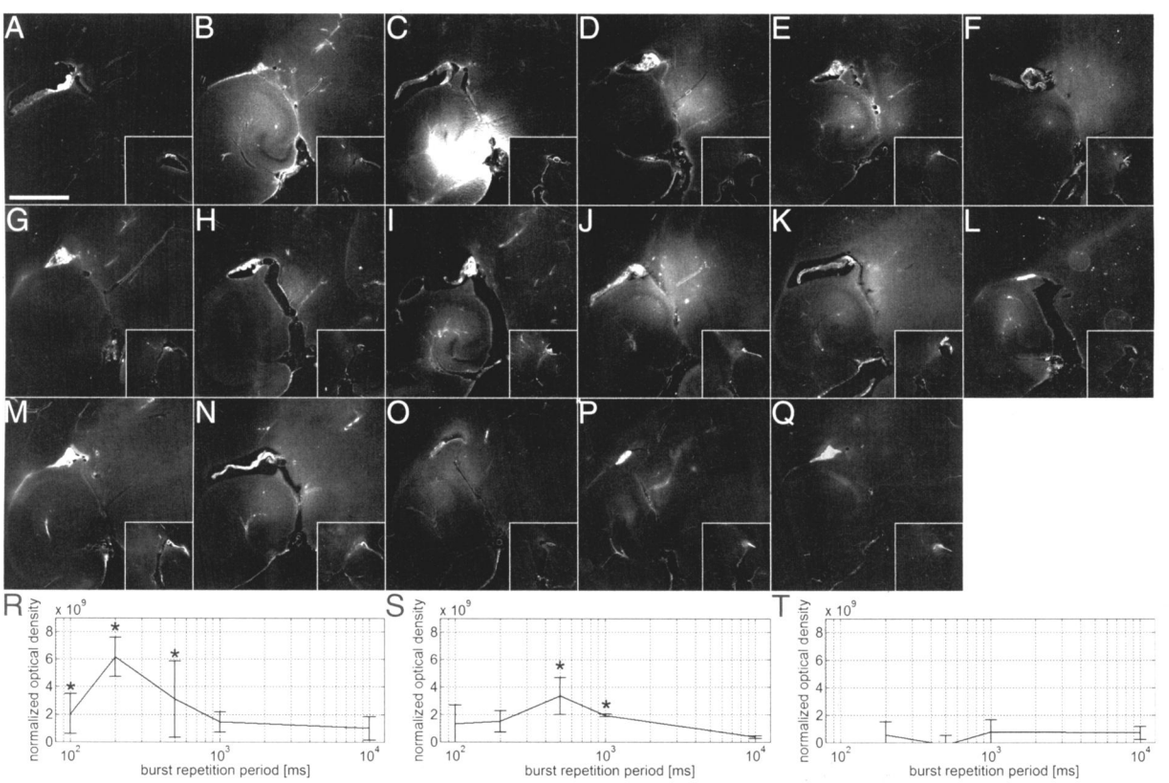

Fig. 1. Fluorescence images and NOD values at different PRFs and BRFs. The left ROI (large boxes in *A–Q*) was sonicated in the presence of microbubbles and fluorescently tagged 3-kDa dextran, whereas the right ROI was a control (small boxes). Sonications were at a PRF of (*A–F* and *R*) 100, (*G–L* and *S*) 25, and (*M–Q*, *T*) 6.25 kHz. The pulse trains were emitted (*A*, *G*, and *M*) continuously or in bursts of 1,000 pulses at a BRF of (*B* and *H*) 10, (*C*, *I*, and *N*) 5, (*D*, *J*, and *O*) 2, (*E*, *K*, and *P*) 1, and (*F*, *L*, and *Q*) 0.1 Hz. An asterisk indicates a significant increase in NOD ($P < 0.05$) relative to sham mice. The bar in *A* depicts 1 mm.

Multisized Dextran. Significant increases in NOD were observed using 3- and 70-kDa dextrans. The 10-kDa dextran was successfully delivered in all three mice, but the increase was not significant ($P = 0.06$). The 3-kDa agent was associated with the most homogeneous distribution across a larger area than the other two molecular weights (Fig. 3*A*). The distribution of 10 kDa was also diffuse, but did not spatially extend to the same degree as the 3-kDa dextran (Fig. 3*B*). The 70-kDa dextran exhibited heterogeneous spots of high levels of fluorescence in combination with diffusely distributed fluorescence (Fig. 3*C*).

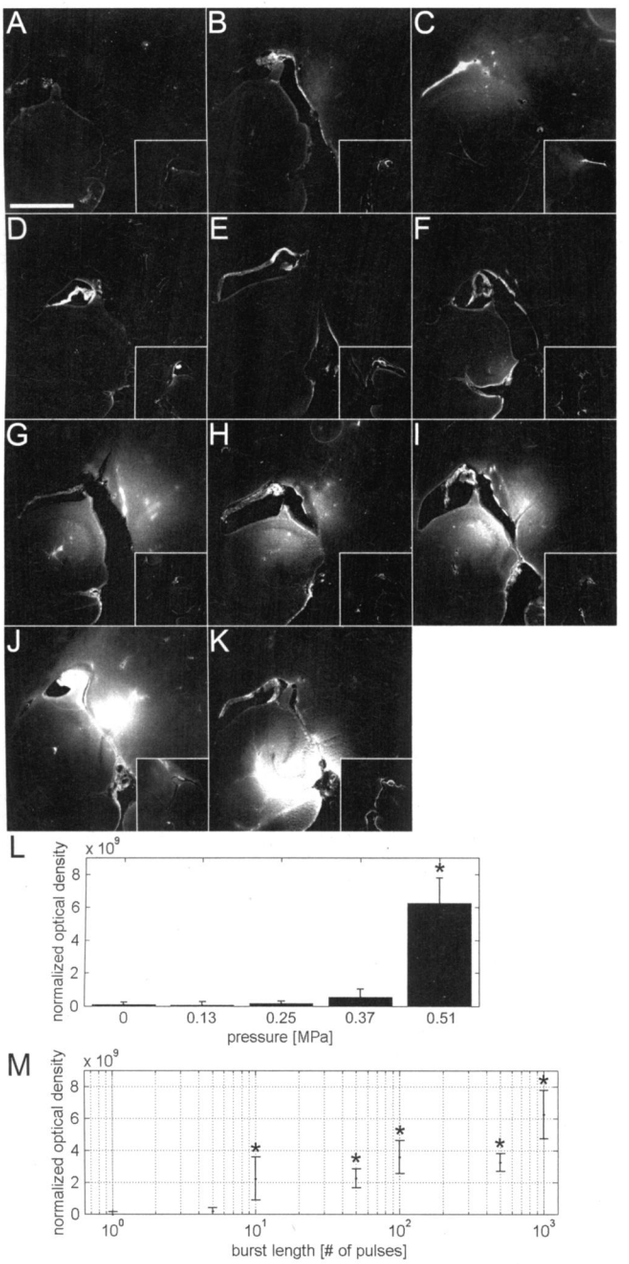

Fig. 2. Fluorescence images and NOD values according to different PRPs and BLs. The left ROI (large boxes in *A–K*) was sonicated in the presence of microbubbles and fluorescently tagged 3-kDa dextran, whereas the right ROI was a control (small boxes). Sonications of a 1,000-pulse BL were emitted at a PRF of 100 kHz and a BRF of 5 Hz using a PRP of (*A*) 0.13, (*B*) 0.25, (*C*) 0.37, and (*K*) 0.51 MPa. (*D*) No sonication was applied in the sham. In the rest of the conditions, pulses were emitted in bursts of (*E*) 1, (*F*) 5, (*G*) 10, (*H*) 50, (*I*) 100, and (*J*) 500 using a 0.51-MPa PRP. The NOD was calculated for each (*L*) PRP and (*M*) BL. An asterisk indicates a significant increase in NOD ($P < 0.05$) relative to (*D*) sham mice. The bar in *A* depicts 1 mm.

Homogeneous Distribution and High Increase in Fluorescence. Certain parameters used in this study produced a fluorescence that was homogeneously distributed in distinct regions within the larger targeted volume. For example, sonication of the ROI using a 25-kHz PRF and a 5-Hz BRF produced a homogeneous distribution of fluorescence throughout the hippocampus, thereby revealing pyramidal cells and the stratum lucidum of CA3 (Fig. 3 *D–F*). This contrast in different anatomical landmarks of the hippocampus was observed with several parameters as shown in Figs. 1–3 using fluorescence microscopy and even in Fig. 4 using MRI. For the case of Fig. 3*E*, the NOD per pixel was greatest in the stratum radium and orien, and significantly different from the stratum lucidium and pyramidale. The stratum pyramidale produced the least NOD per pixel of all four regions. Each one of these four regions had significant increases in NOD per pixel when compared to their corresponding regions in the right hemispheric control. Furthermore, there were cases where, in addition to a homogeneous distribution of fluorescence, an even higher level of fluorescence was observed that outlined the morphology of neurons and/or glial cells, and capillaries. For example, sonica-

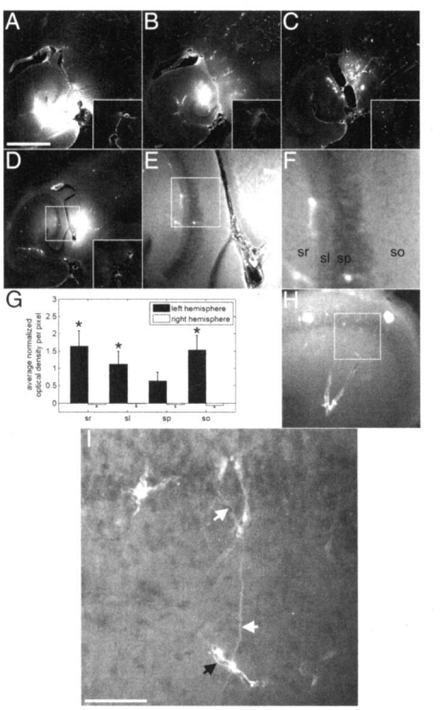

Fig. 3. Fluorescence images depicting delivery of dextrans at distinct molecular weights, spatially homogenous delivery, and outlines of neuronal axons. The left ROI of the brain was sonicated in the presence of microbubbles and fluorescently tagged (*A*, *D–F*, *H* and *I*) 3-, (*B*) 10-, and (*C*) 70-kDa dextrans. Diffuse fluorescence regions can be observed for all dextrans, whereas spots of high fluorescence are observed only with the 70-kDa dextran. Pulsing in bursts using a 3.5-cycle pulse length allowed for a (*D–F*) homogeneous and diffuse spatial distribution of 3-kDa dextran to the target ROI. *F* is a zoomed image of the white square in *E*, which is subsequently a zoomed image of the white square in *D*. (*G*) Subregions within the hippocampus displayed difference in NOD. sr, stratum radiatum; sl: stratum lucidum; sp: stratum pyramidale; so: stratum orien. (*H* and *I*) In some brains, the morphology of neurons and vessels can be observed to have increased fluorescence over high levels of diffuse fluorescence. *I* is a zoomed image of *H* using confocal microscopy. Here, axons (white arrows) and a capillary (black arrow) are observed. The bar in *A* and *I* depicts 1 mm and 50 μm, respectively. An asterisk indicates a significant increase in left hemispheric NOD per pixel ($P < 0.05$) relative to the stratum pyramidale.

tion of the left ROI at a 100-kHz PRF, a 1,000-pulse BL, and a 2-Hz BRF had both a significant increase in NOD in the entire region shown in Fig. 3*H* and Movies S1 and S2, and a clear delineation of an axon with an approximate diameter of 1 μm that extended from its cellular body and attached to a capillary, with a diameter of approximately 4.5 μm.

Magnetic Resonance Imaging. Dynamic contrast-enhanced MRI depicted gadolinium being spatially distributed throughout the targeted volume (Fig. 4 *A–C*) and was reproducible in all mice. No observable bias was observed near the dorsal skull region. The permeability value to the systemically administered contrast agent was also calculated (Fig. 4 *D–K*) and the K_{trans} was found to be 0.022 ± 0.013 min^{-1}.

Histological Analysis. With H&E, three histological measures were used: the number of dark neurons, erythrocyte extravasation sites, and microvacuolations (Fig. S3). Overall, damage was limited to a few scattered dark neurons, mainly located in the pyramidal and granular cell layers of the hippocampus. However, there was no difference between the target and control regions. Microvacuolations and erythrocyte extravasation sites were not detected. There was no difference in the number of TUNEL-positive cells present in the two hemispheres.

Discussion

The results shown in this paper introduce a previously undescribed basis for pulse-sequence designing for FUS-based DDSs and offer insight into the mechanism of increased vascular permeability. Previous work by our group and others typically optimized a few ultrasonic parameters, namely the PRP, frequency, PRF, and PL. However, increasing the delivered dose by modifying one of these parameters was also associated with either poorer distribution characteristics (17) or the onset of cellular damage (11). This paper explored a wider range of parameters that, to our knowledge, has not been used for drug delivery. The choice of pulse sequences to explore was based on the hypothesis that extravasations of molecules through BBB disruption can be enhanced not only by the type and magnitude of cavitation, but also by the number and location of cavitation events throughout the cerebral microvasculature. By incorporating concepts of microbubble persistence, fragmentation, and microvascular replenishment, the aim in this study was to concentrate the majority of the acoustic cavitation activity within the microvasculature as opposed to the larger vessel branches. This was achieved by grouping a series of short pulses into a burst, which allowed a sufficient time interval between bursts to allow for microbubble replenishment of the microvasculature before the arrival of the subsequent acoustic pulses. This basis of inducing BBB disruption resulted in a higher dose and homogeneous distribution of molecular delivery without conventional trade-offs in safety.

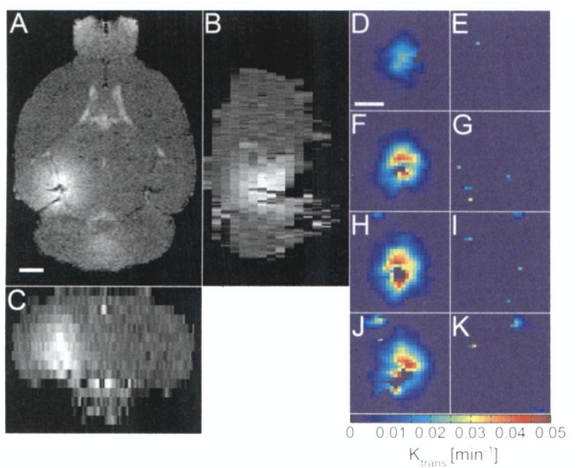

Fig. 4. MRI of the mouse brain and permeability maps. The left ROI of the brain was sonicated in the presence of microbubbles and the right ROI served as the control. Sequential T1-weighted MRI was acquired after intraperitoneal injection of gadolinium, which normally does not permeate the BBB. (*A*) Horizontal, (*B*) sagittal, and (*C*) coronal orientations depict a good distribution of gadolinium throughout the targeted ROI relative to the control ROI. Permeability maps of the (*D*, *F*, *H*, and *J*) targeted and (*E*, *G*, *I*, and *K*) control ROIs are depicted in several horizontal planes, increasingly ventral.

Ultrasound and Microbubble Parameters Necessary for BBB Disruption. This paper has elucidated evidence in identifying the essential ultrasonic parameters that disrupt the BBB, which may be of use not only for methods that aim at enhancing drug delivery, but also those that intend to avoid it (e.g., diagnostic imaging, sonothrombolysis, and encapsulated drug release). First, BBB disruption requires a sufficiently high PRP. In this paper, a significant increase did not occur until 0.51 MPa, although incidences of increased NOD were observed at as low as 0.13 MPa. A PRP threshold has been previously shown (2, 14), and the present study also confirms it at short PLs. Second, previous work has demonstrated that lower center frequencies (e.g., 0.25 and 0.6 MHz) reduce the PRP threshold of BBB disruption (15, 18). Third, effective BBB disruption requires a time interval where no ultrasound was emitted (i.e., intervals between pulses or bursts). In this paper, this value fell between 0.1 and 1 s in duration, and any further increase or decrease in duration reduced the extent of BBB disruption. Finally, a minimum number of acoustic cycles needs to be transmitted to the tissue as either a series of short pulses or a long continuous pulse. In this paper, we demonstrated that BBB disruption may be achieved with as little as 5 pulses of 3.5 cycles (2.3 μs at 1.5 MHz) transmitted at a PRF of 100 kHz. Our previous work has demonstrated that 50 cycles (33 μs at 1.5 MHz) can induce BBB disruption (16). Increasing the number of emitted pulses, or the PL, increased the NOD.

The total ultrasonic energy administered through changes to the PRP (Fig. 2*L*) and number of pulses emitted (Fig. 2*M*) was shown to influence the NOD. However, the highest energy administered with continuous pulses (PRF: 100 kHz, total number of pulses: 66,000,000) produced no NOD increase, whereas the highest NOD achieved was with a 20-factor reduction in the pulses emitted (PRF: 100 kHz, BRF: 5 Hz, total number of pulses: 3,300,000). On the other hand, decreasing the PRF from 100 to 6.25 kHz, while maintaining constant energy, reduced the NOD to a level indistinguishable from the sham case. These findings may be due to microbubble depletion through uninterrupted pulsed sonication and long pulse interval durations.

To date, a wide class of albumin- and lipid-shelled as well as polydispersed and size-isolated microbubbles have been utilized and include Optison (1), SonoVue (19), Definity (2), and custom-designed microbubbles (9, 20). Recent studies have shown that larger microbubbles (4–5 and 6–8 μm) have a lower PRP threshold for BBB disruption than smaller bubbles (1–2 μm) (9, 20) when using PLs greater than 66.7 μs. Also, previous work, which analyzed concentrations of 0.01 to 0.25 μL/g, did not show any significant differences in drug delivery concentration (16), which was in good agreement with other studies that used similar parameters (15).

Mechanism of Brain Drug Delivery. A microbubble radially expands and contracts in response to the acoustic pressure rarefaction and compression, respectively. At low PRPs, this may lead to stable radial oscillations that continue over several cycles, possibly leading to bubble growth through rectified diffusion or shrinkage leading to dissolution. At high PRPs, the bubble can expand to several times its equilibrium radius and then collapse due to the inertia of the surrounding medium. Both stable and inertial

cavitation have been observed to both mechanically agitate the microvascular wall (8) and cause extravasation of vascular agents (7, 21). Previous reports using longer PLs of 10 or 20 ms have analyzed the acoustic emissions radiating from the acoustically driven microbubbles and have indicated that BBB disruption may occur with stable cavitation or nonviolent inertial cavitation (22–23). However, it is difficult to infer to the type of cavitation activity present in our experiments due to the shorter duration of the PL used and the fact that we are operating at PRPs near the threshold of BBB disruption.

The pulse sequence designed in this paper was based on the hypothesis that BBB disruption is dependent on the higher probability and extent of cavitation events occurring along the cerebral microvessels. This guiding hypothesis led to the discovery of a previously undescribed basis for the ultrasound pulse-sequence design for brain drug delivery presented here. Most striking is that, despite the short pulse employed, increasing the number of pulses emitted increased the NOD level (Fig. 2*M*). However, it is not clear whether this increase in fluorescence is due to the number of disrupted sites or the magnitude of disruption at each site. Regardless, emitting pulses in bursts, as opposed to in a long PL, may generate greater microbubble mobility and allow a single bubble to undergo cavitation at multiple sites along the cerebral microvessel as it moves between pulses. The persistence of a microbubble stimulated over several rapidly emitted pulses has been previously demonstrated by other groups in tunnel phantoms and microvessel models (8), and a similar phenomenon may be occurring in our present study. In addition, bursts of short PLs could allow for increased mobility due to reduced radiation force effects. As a result, we believe that it is this increased number of BBB-disrupted sites as opposed to the magnitude of disruption that is facilitating an increase in the dose and allows for a more homogenous drug delivery distribution. Further studies are currently ongoing to verify this observation.

Enhancement of Drug Delivery Without Compromising Safety. FUS-induced BBB disruption has been previously demonstrated to successfully deliver large molecular agents such as 70-kDa dextrans (17), Herceptin (24), and Doxorubicin (25). Nevertheless, concerns remain with the dose and distribution of the agents delivered (14, 17) and the safety associated with enhancing these characteristics (11). For instance, increased dose can be achieved with higher PRPs and PLs, but higher PRPs have been associated with cellular damage (11) and longer PLs have been associated with increased molecular accumulation at or near larger vessels, thus indicating off-target and inhomogeneous distribution (16, 17). The short PL sequences used in this paper produced a more homogeneous distribution of molecular delivery throughout the targeted volume when compared to longer 20-ms PLs, especially for the 3-kDa dextran (Figs. 1 and 2). However, drug penetration and distribution are a greater concern for larger molecular weight agents because attempts to deliver 70-kDa dextran using a 20-ms PL resulted in punctate regions of high concentrations in the larger vessels (i.e., longitudinal and transverse hippocampal vessels and posterior cerebral artery) in addition to low levels of diffuse fluorescence (17). Although short PLs have not eliminated the presence of these punctate regions, evidence suggests that their locations have penetrated deeper into the vascular branches and into smaller vessels such as arterioles. This feature was complemented by high levels of diffuse fluorescence throughout the target regions, thus showing greater promise for larger therapeutic agents (Fig. 3*C*). In addition, our previous work using 20-ms-PL pulses and a gadolinium-based MRI contrast agent depicted a similarly high concentration at or near larger vessel branches, most notably along the transverse hippocampal vessels in the form of a curve extending clockwise from the posterior cerebral artery and into the hippocampal formation (14). This spatial bias was absent in all cases evaluated in the present study using short PLs (Fig. 4).

The higher dose and improved distribution of dextran throughout the targeted region resulted in previously undescribed observations. First, in the instances where the dose and distribution were markedly enhanced, several hippocampal landmarks, most notably the stratum radiatum, increased in fluorescence at different amounts (Fig. 3 *D–F*). The apparent contrast in fluorescence is most likely due to differences in the dose of dextran delivered in each respective region, which suggests region-specific variables, such as capillary density, orientation (i.e., vessels are parallel or perpendicular to the beam propagation), enzymatic activity, and extracellular space diffusion coefficient. Still, there was a significant increase in every region when compared to its respective right region (Fig. 3*G*), indicating utility of FUS-based drug delivery for a wide range of cellular targets. In other instances, we were able to observe delineation of the morphology of neuronal or glial processes and capillaries. It remains uncertain how they became fluorescent, whether due to actual neuronal uptake or whether the dextran simply attached to the extracellular space near the membrane. Ultimately, we have shown that a molecular agent was successfully delivered across the BBB and to potential therapeutic targets, such as neurons and glial cells.

Initial histological evaluation of the short-PL-based pulse sequences suggests a level of safety for the DDS because no differences were observed when comparing the targeted region to the control hippocampus. During H&E analysis, microvacuolations and erythrocyte extravasation sites were not detected in any of the sections. Although a few dark neurons were observed in the hippocampus, they were found in both the target and control hemispheres. No obvious increase in TUNEL-positive cells was observed in the targeted hemisphere versus the control. Although the parameters allowed for a high dose and distribution of dextran, no significant damage was observed. Enhancement without damage may be due to an increased number of BBB disruption sites with the same magnitude of cavitation activity.

Clinical Implications. One of the advantages of FUS-induced BBB disruption is the ability to noninvasively, locally, and transiently deliver agents to a target ROI. Large molecules of 3, 10, and 70 kDa were delivered to the left hippocampus, which is relevant for several drugs such as bace-1 inhibitors and brain-derived neurotrophic factors. Nevertheless, transcranial ultrasound propagation while maintaining a tight focus and a safety level remains a challenge. One solution uses computed tomography (CT)-based bone density maps to correct for aberrations due to the skull (26). However, it is complicated and expensive requiring a high-resolution CT scan, and subsequently necessitating radiation exposure. Because lower ultrasound frequencies are less aberrated by the skull and tissue, less distortion to the focus through the skull will occur (27). However, this same property increases its ability to reflect within the skull and thus generate standing waves when the PL is long. At 500 kHz, a 10-ms PL is 5,000 m long. In contrast, a three-cycle PL is only 9 mm at 500 MHz. Our short PLs at low PRFs may allow for reduction or elimination of standing waves and thus generate (1) more predictable acoustic pressure fields and (2) avoid reduced cavitation threshold generated by nodes and antinodes.

This study determined a basis for ultrasonic parameters necessary for BBB disruption. Specifically, a sufficient number of pulses need to interact with microbubbles within the vasculature at a sufficiently large PRP. The short PL-based pulse sequences described in this paper delivered a high dose of dextran homogenously throughout the targeted region. In certain instances, this allowed for hippocampal anatomical landmarks and the morphology of neurons to be highlighted, further demonstrating delivery to or into cells of various regions within the focal volume. These drug delivery characteristics were enhanced in the absence

of detectable erythrocyte extravasation and neuronal damage, as assessed by the amount of apoptotic neurons. This basis may not only help enhance drug delivery in other organs beyond BBB disruption, but also improve safety by avoiding BBB disruption with other technologies such as diagnostic ultrasound imaging.

Materials and Methods

Animals. Each of the 95 C57Bl6 male mice (23.8 ± 1.7 g, Harlan Laboratories) were anesthetized with a mixture of oxygen (0.8 L/min at 1.0 bar, 21 °C) and 1.5–2.0% vaporized isoflurane (Aerrane, Baxter Healthcare) using an anesthesia vaporizer (SurgiVet, Smiths Group) while respiration rates were continuously monitored. The Columbia University Institutional Animal Care and Use Committee approved all mouse studies presented.

Ultrasound Equipment and Targeting Procedure. A single-element, spherical-segment FUS transducer (center frequency: 1.5 MHz, focal depth: 60 mm, diameter: 60 mm; Imasonic) was driven by a function generator (33220A, Agilent) through a 50-dB power amplifier (325LA, E&I). A pulse-echo transducer (center frequency: 10 MHz; focal length 60 mm; Olympus) was positioned through a central hole of the FUS transducer so that their foci were aligned and was driven by a pulser-receiver system (Olympus) connected to a digitizer (Gage Applied Technologies). A chamber filled with degassed and distilled water was mounted on the transducer system and sealed with an acoustically transparent latex membrane (Trojan; Church & Dwight Co). The transducers were attached to a three-dimensional positioning system (Velmex).

The mouse head was immobilized and fur on the head was removed. A water container with an acoustically and optically transparent base was placed on the head and coupled with ultrasound gel. The FUS transducer was moved 2.5 mm lateral of the sagittal suture and 2.0 mm anterior of the lambdoid suture using a previously described grid positioning method (1) so that its focus overlapped the left ROI (Fig. S2).

Microbubble and Dextran Formulation. Definity microbubbles (concentration: 0.05 μL/g of body mass, diameter: 1.1–3.3 μm, vial concentration: 1.2×10^{10} bubbles/mL; Lantheus Medical Imaging) were mixed in 100 μL of PBS. In brains analyzed for fluorescence, lysine-fixable, Texas red-tagged dextran (concentration: 60 μg/g of body mass, molecular weight: 3, 10, or 70 kDa) were dissolved in the solution. The solution was then injected into the tail vein during 30 s.

Acoustic Parameters. The left brain ROI of each mouse was exposed to 1 of 27 ultrasonic exposure conditions (Table S1) while the right ROI remained unsonicated (Fig. S2). Each condition was repeated in three different mice. In one of the conditions, mice underwent a sham whereby all procedures were performed except for the sonication. In all other conditions, a 3.5-cycle pulse with a 1.5-MHz center frequency was used. Unless otherwise noted, a 0.51-MPa PRP, 100-kHz PRF, 5-Hz BRF, and 1000 BL were used. At 6.25-kHz PRF, mice were pulsed without bursting and with bursts at BRFs of 5, 2, 1, and 0.1 Hz. At 25- and 100-kHz PRFs, mice were pulsed without bursting and with burst at BRFs of 10, 5, 2, 1, and 0.1 Hz. BLs were evaluated at 1, 5, 10, 50, 100, 500, and 1,000 pulses while PRPs were evaluated at 0.13, 0.25, 0.37, and 0.51 MPa.

Statistical Analysis. Occurrence of delivery was determined if the NOD in a sonicated mouse was greater than a standard deviation above the NOD in sham mice and was confirmed qualitatively. One-way ANOVA was performed to determine whether all groups were the same, and multiple comparisons were performed using Tukey's least significant difference methods to determine differences in magnitude among the experimental conditions. Data are reported as mean ± standard deviations (Table S1) and values of $P \leq 0.05$ were considered significant.

ACKNOWLEDGMENTS. The authors thank Dr. Barclay Morrison III, PhD, for discussions on the identification of neurons and capillaries and Derrick Wang for fluorescence imaging of some brain sections. This study was supported by the National Institutes of Health (R01 EB009041), National Science Foundation (CAREER 0644713), and the Kinetics Foundation.

1. Choi JJ, Pernot M, Small SA, Konofagou EE (2007) Noninvasive, transcranial and localized opening of the blood-brain barrier using focused ultrasound in mice. *Ultrasound Med Biol* 33:95–104.
2. Hynynen K, McDannold N, Vykhodtseva N, Jolesz FA (2001) Noninvasive MR imaging-guided focal opening of the blood-brain barrier in rabbits. *Radiology* 220:640–646.
3. Lin CY, et al. (2010) Quantitative and qualitative investigation into the impact of focused ultrasound with microbubbles on the triggered release of nanoparticles from vasculature in mouse tumors. *J Control Release* 146:291–298.
4. Mayer CR, Bekeredjian R (2008) Ultrasonic gene and drug delivery to the cardiovascular system. *Adv Drug Deliv Rev* 60:1177–1192.
5. Fischer K, et al. (2009) Renal ultrafiltration changes induced by focused US. *Radiology* 253:697–705.
6. Apfel RE (1997) Sonic effervescence: A tutorial on acoustic cavitation. *J Acoust Soc Am* 101:1227–1237.
7. Raymond SB, Skoch J, Hynynen K, Bacskai BJ (2007) Multiphoton imaging of ultrasound/Optison mediated cerebrovascular effects in vivo. *J Cereb Blood Flow Metab* 27:393–403.
8. Caskey CF, Stieger SM, Qin S, Dayton PA, Ferrara KW (2007) Direct observations of ultrasound microbubble contrast agent interaction with the microvessel wall. *J Acoust Soc Am* 122:1191–1200.
9. Choi JJ, et al. (2010) Microbubble-size dependence of focused ultrasound-induced blood-brain barrier opening in mice in vivo. *IEEE Trans Biomed Eng* 57:145–154.
10. Samuel S, Cooper MA, Bull JL, Fowlkes JB, Miller DL (2009) An *ex vivo* study of the correlation between acoustic emission and microvascular damage. *Ultrasound Med Biol* 35:1574–1586.
11. Baseri B, Choi JJ, Tung YS, Konofagou EE (2010) Multi-modality safety assessment of blood-brain barrier opening using focused ultrasound and definity microbubbles: A short-term study. *Ultrasound Med Biol* 36:1445–1459.
12. Miller DL, Quddus J (2000) Diagnostic ultrasound activation of contrast agent gas bodies induces capillary rupture in mice. *Proc Natl Acad Sci USA* 97:10179–10184.
13. Reinhard M, et al. (2006) Blood-brain barrier disruption by low-frequency ultrasound. *Stroke* 37:1546–1548.
14. Choi JJ, Pernot M, Brown TR, Small SA, Konofagou EE (2007) Spatio-temporal analysis of molecular delivery through the blood-brain barrier using focused ultrasound. *Phys Med Biol* 52:5509–5530.
15. McDannold N, Vykhodtseva N, Hynynen K (2008) Blood-brain barrier disruption induced by focused ultrasound and circulating preformed microbubbles appears to be characterized by the mechanical index. *Ultrasound Med Biol* 34:834–840.
16. Choi JJ, et al. (2011) Noninvasive and localized blood-brain barrier disruption using focused ultrasound can be achieved at short pulse lengths and low pulse repetition frequencies. *J Cereb Blood Flow Metab* 31:725–737.
17. Choi JJ, Wang S, Tung YS, Morrison B, 3rd, Konofagou EE (2010) Molecules of various pharmacologically-relevant sizes can cross the ultrasound-induced blood-brain barrier opening in vivo. *Ultrasound Med Biol* 36:58–67.
18. Hynynen K, et al. (2006) Focal disruption of the blood-brain barrier due to 260-kHz ultrasound bursts: A method for molecular imaging and targeted drug delivery. *J Neurosurg* 105:445–454.
19. Choi JJ, et al. (2008) Noninvasive and transient blood-brain barrier opening in the hippocampus of Alzheimer's double transgenic mice using focused ultrasound. *Ultrason Imaging* 30:189–200.
20. Vlachos F, Tung YS, Konofagou E (2011) Permeability dependence study of the focused ultrasound-induced blood-brain barrier opening at distinct pressures and microbubble diameters using DCE-MRI. *Magn Reson Med* 66:821–830.
21. Stieger SM, et al. (2007) Enhancement of vascular permeability with low-frequency contrast-enhanced ultrasound in the chorioallantoic membrane model. *Radiology* 243:112–121.
22. Tung YS, Choi JJ, Baseri B, Konofagou EE (2010) Identifying the inertial cavitation threshold and skull effects in a vessel phantom using focused ultrasound and microbubbles. *Ultrasound Med Biol* 36:840–852.
23. Tung YS, et al. (2010) In vivo transcranial cavitation threshold detection during ultrasound-induced blood-brain barrier opening in mice. *Phys Med Biol* 55:6141–6155.
24. Kinoshita M, McDannold N, Jolesz FA, Hynynen K (2006) Noninvasive localized delivery of Herceptin to the mouse brain by MRI-guided focused ultrasound-induced blood-brain barrier disruption. *Proc Natl Acad Sci USA* 103:11719–11723.
25. Treat LH, et al. (2007) Targeted delivery of doxorubicin to the rat brain at therapeutic levels using MRI-guided focused ultrasound. *Int J Cancer* 121:901–907.
26. Aubry JF, Tanter M, Pernot M, Thomas JL, Fink M (2003) Experimental demonstration of noninvasive transskull adaptive focusing based on prior computed tomography scans. *J Acoust Soc Am* 113:84–93.
27. Deffieux T, Konofagou EE (2010) Numerical study of a simple transcranial focused ultrasound system applied to blood-brain barrier opening. *IEEE Trans Ultrason Ferroelectr Freq Control* 57:2637–2653.